



## Exploring the roles of oxygen species in H<sub>2</sub> oxidation at $\beta$ -MnO<sub>2</sub> surfaces using operando DRIFTS-MS

Jiacheng Xu<sup>1,2</sup>, Tiantian Zhang<sup>1</sup>, Shiyu Fang<sup>1</sup>, Jing Li<sup>1,3</sup>, Zuliang Wu<sup>1,3</sup>, Wei Wang<sup>1,3</sup>, Jiali Zhu<sup>1,3</sup>, Erhao Gao<sup>1,3</sup> & Shuiliang Yao<sup>1,2,3</sup>  

Understanding of the roles of oxygen species at reducible metal oxide surfaces under real oxidation conditions is important to improve the performance of these catalysts. The present study addresses this issue by applying a combination of operando diffuse reflectance infrared Fourier transform spectroscopy with a temperature-programmed reaction cell and mass spectrometry to explore the behaviors of oxygen species during H<sub>2</sub> oxidation in a temperature range of 25–400 °C at  $\beta$ -MnO<sub>2</sub> surfaces. It is revealed that O<sub>2</sub> is dissociated simultaneously into terminal-type oxygen (M<sup>2+</sup>-O<sup>2-</sup>) and bridge-type oxygen (M<sup>+</sup>-O<sup>2-</sup>-M<sup>+</sup>) via adsorption at the Mn cation with an oxygen vacancy. O<sub>2</sub> adsorption is inhibited if the Mn cation is covered with terminal-adsorbed species (O, OH, or H<sub>2</sub>O). In a temperature range of 110–150 °C, OH at Mn cation becomes reactive and its reaction product (H<sub>2</sub>O) can desorb from the Mn cation, resulting in the formation of bare Mn cation for O<sub>2</sub> adsorption and dissociation. At a temperature above 150 °C, OH is reactive enough to leave bare Mn cation for O<sub>2</sub> adsorption and dissociation. These results suggest that bare metal cations with oxygen vacancies are important to improve the performance of reducible metal oxide catalysts.

<sup>1</sup>School of Environmental and Safety Engineering, Changzhou University, Changzhou, China. <sup>2</sup>School of Material Science and Engineering, Changzhou University, Changzhou, China. <sup>3</sup>Advanced Plasma Catalysis Engineering Laboratory for China Petrochemical Industry, Changzhou, China. ✉email: [yaos@cczu.edu.cn](mailto:yaos@cczu.edu.cn)

Oxygen vacancy (OV) defects at reducible metal oxide surfaces play a key role in a heterogeneous catalytic oxidation process<sup>1–4</sup>. In 1954, Mars and van Krevelen reported that the oxidation of organic compounds on  $V_2O_5$  includes  $V_2O_5$  reduction by an organic compound and the subsequent oxidation of  $V_2O_5$  by  $O_2$ <sup>5</sup>. This reduction and oxidation mechanism had been verified the OVs at the atomic level for the oxidation of CO on  $RuO_2$  (110) surfaces using scanning tunneling microscopy (STM) in conjunction with density-functional theory (DFT) calculations<sup>6</sup>. This has induced a boost in studies to identify OVs on metal oxide surfaces. For example, OVs have been identified on the surfaces of rutile  $TiO_2$  using high-resolution STM<sup>7</sup>. Other studies have demonstrated that many types of OVs with different catalytic reaction characteristics can exist on metal oxide surfaces. OVs have been observed on metal oxide surfaces in association with three metal (M) and oxygen (O) groups (M=O, M–O–M, and  $M_3$ –O)<sup>8</sup>. Moreover, the local structures of OVs on the treated and untreated surfaces of  $CeO_2$  (110) crystal planes have been elucidated using STM in conjunction with DFT calculations<sup>9</sup>.

Recent reviews have summarized the methods that can be applied to characterize oxygen species at catalyst surfaces<sup>10</sup> (Supplementary Table S1). An overview has focused on understanding the roles of OVs playing in the oxidation reaction at reducible metal oxide surfaces<sup>11</sup>. For example, the dissociation of  $O_2$  at OVs was found to greatly impact oxygen adsorption on  $TiO_2$  (110) surfaces, where one O atom from the dissociated  $O_2$  molecule is postulated to fill an OV and the second O atom deposited at the five-coordinate  $Ti^{4+}$  site<sup>12</sup>. The roles of oxygen atoms and molecules at catalyst surfaces and the properties of OVs have also been the subject of a recent review<sup>13</sup>.

The importance of OVs has led to the development of numerous strategies for increasing the concentration of OVs in metal oxide catalysts. Some success has been achieved via doping with secondary metal ions and nano structuring<sup>14,15</sup>, and the doping strategy has been expanded to develop four-layer metal oxide catalysts ( $CuO/VO_x/Ti_{0.5}Sn_{0.5}O_2$ ) with layers composed of synergistic OV concentrations<sup>16</sup>. The dispersal of metal ions on the surfaces of metal oxides has also been demonstrated to increase the concentration of OVs effectively<sup>17,18</sup>. These strategies have been widely used in photocatalytic materials, electrocatalytic materials, thermal catalytic materials, and optical materials<sup>19–21</sup>. However, effective methods to improve the performance of metal oxide catalysts are influenced by current characterization technologies. Therefore, it is required to find an effective characterization technology to identify OVs and understand oxidation mechanisms that occur at the surfaces of metal oxides under real reaction conditions.

The operando diffuse reflectance infrared Fourier transform spectroscopy (DRIFTS) is a powerful technology that can identify surface species on a catalyst under real reaction conditions. Ye et al. found that toluene adsorption and reaction with OVs can effectively reduce the accumulation of by-products<sup>22</sup>. Li et al. investigated the structure-performance relationships of  $\alpha$ ,  $\beta$ ,  $\gamma$ , and  $\delta$ - $MnO_2$  catalysts, they found that toluene adsorption is promoted by rapid dehydrogenation of methyl groups on the surface of  $\delta$ - $MnO_2$ <sup>23</sup>. Yao et al. used the combination of DRIFTS with a mass spectrometry (MS) to observe the functional groups on the catalyst surface and the changes in MS signals of gaseous components during the catalytic oxidation of toluene on  $CeO_2$ <sup>24</sup>.

Due to its multiple valence states and structural diversity (e.g., tunneling ( $\alpha$ ,  $\beta$ , and  $\gamma$ - $MnO_2$ ) and layered ( $\delta$ - $MnO_2$ ) structures),  $MnO_2$  is an important functional metal oxide material<sup>25–27</sup>.  $\beta$ - $MnO_2$  has a thermodynamically stable phase and high crystallinity, and become one of the hot spots in current researches<sup>28,29</sup>.

The present work addresses these issues by combining an operando DRIFTS with a temperature-programmed reaction (TPR) cell and MS to explore the behaviors of OVs and adsorbed oxygen species at  $\beta$ - $MnO_2$  surfaces during  $H_2$  oxidation reaction conducted in the temperature range of 25–400 °C. The roles of OVs in  $H_2$  oxidation process are explored according to relations between OVs and oxygen species, which in turn reveal interactions between surface oxygen species with  $H_2$  at different reaction temperatures.

## Results and discussion

**Catalyst characterization.** The crystal structure of  $\beta$ - $MnO_2$  was confirmed using X-ray diffraction (XRD).  $\beta$ - $MnO_2$  has good crystallization and no obvious crystal defects (Fig. 1a). High-resolution transmission electron microscope (HRTEM) image of  $\beta$ - $MnO_2$  is shown in Supplementary Fig. S1. The well-identified periodic lattice fringes of 2.41 and 3.15 nm are corresponding to the interplanar distances of (101) and (110) facets of  $\beta$ - $MnO_2$ . Whereas severe blurring of the lattice fringes is also found (highlighted by red rectangles), suggesting the existence of OVs at  $\beta$ - $MnO_2$  surfaces<sup>30</sup>.

Figure 1b shows the Raman scattering spectrum of  $\beta$ - $MnO_2$ . The band at 630  $cm^{-1}$  corresponds to the tensile pattern of the  $[MnO_6]$  octahedron, and the band at 330  $cm^{-1}$  is assigned to the metal-oxygen chain of Mn–O–Mn in the  $MnO_2$  octahedral lattice, indicating the presence of a well-developed rutile-shaped skeleton<sup>31</sup>.

Thermogravimetric (TG) analysis result shows that the weight loss of  $\beta$ - $MnO_2$  is not obvious below 500 °C (Fig. 1c). This is due to the coordination of Mn and O in the phase structure is close to saturation, and the phase tunnel structure is stable. The weight loss at higher temperatures is attributed to the removal of lattice oxygen, resulting in the reduction of  $MnO_2$  to  $Mn_2O_3$  (between 500 and 600 °C) with a weight loss of 9.63% and to  $Mn_3O_4$  (between 720 and 820 °C) with a weight loss of 3.62%<sup>32</sup>.

$O_2$  temperature-programmed desorption ( $O_2$ -TPD) was used to observe the  $O_2$  desorption from  $\beta$ - $MnO_2$  (Fig. 1d). There is a small desorption peak around 150 °C, which is a signal of surface oxygen desorption. When the temperature reaches about 587 and 813 °C, two obvious desorption peaks appear. The small peak at around 150 °C is due to  $O_2$  desorbed from  $\beta$ - $MnO_2$ , the peaks at 587 and 813 °C are related to the desorption of lattice oxygen and bulk lattice oxygen<sup>33,34</sup>.

X-ray photoelectron spectroscopy (XPS) was used to measure the valence states of Mn and the types of O at  $\beta$ - $MnO_2$  surfaces (Fig. 1e, f and Table 1). The fraction ratios of  $Mn^{3+}$  and  $Mn^{4+}$  are 32.0% and 68.0%, respectively, indicating that  $\beta$ - $MnO_2$  is oxidizable and reducible.  $O_{1s}$  spectrum can be divided into lattice oxygen ( $O_{latt}$ ) at 529.2 eV and adsorbed oxygen/surface hydroxyl groups ( $O_{ads}$  and  $(OH)_{ads}$ ) at 531.7 and 533.2 eV (Fig. 1f)<sup>35,36</sup>. The fraction ratio of  $O_{latt}$  is 77.2%, indicating the presence of OVs at  $\beta$ - $MnO_2$  surface.

## $H_2$ oxidation by surface oxygen species in the absence of $O_2$ .

The DRIFTS spectra, MS signals, and normalized peak intensities during  $H_2$  oxidation by oxygen species at  $\beta$ - $MnO_2$  surfaces in the absence of  $O_2$  are shown in Fig. 2. Seven kinds of oxygen species at  $\beta$ - $MnO_2$  surfaces can be found, those are bridge-type ( $M^{+}-O^{2-}-M^{+}$ ) group (750–800  $cm^{-1}$ )<sup>37</sup>, terminal-type ( $M^{2+}-O^{2-}$ ) group (1300–1400  $cm^{-1}$ )<sup>38–40</sup> (Supplementary Figs. S2–S4 also prove that 1300  $cm^{-1}$  belongs to M=O at  $\beta$ - $MnO_2$  surfaces),  $M^{+}-O^{-}$  group (870  $cm^{-1}$ )<sup>41</sup>, adsorbed molecular  $O_2$  groups including  $M^{+}-O_2^{-}$  group (1110–1120  $cm^{-1}$ )<sup>42,43</sup> and  $M^{2+}-O_2^{2-}$  group (930–960  $cm^{-1}$ )<sup>44</sup>, and oxidation products including  $\delta(H_2O)$  (1520, 1610, and 1640  $cm^{-1}$ ) and  $\nu(OH)$  (3080, 3230, 3530, and 3720  $cm^{-1}$ )<sup>45,46</sup> (Supplementary Table S3).

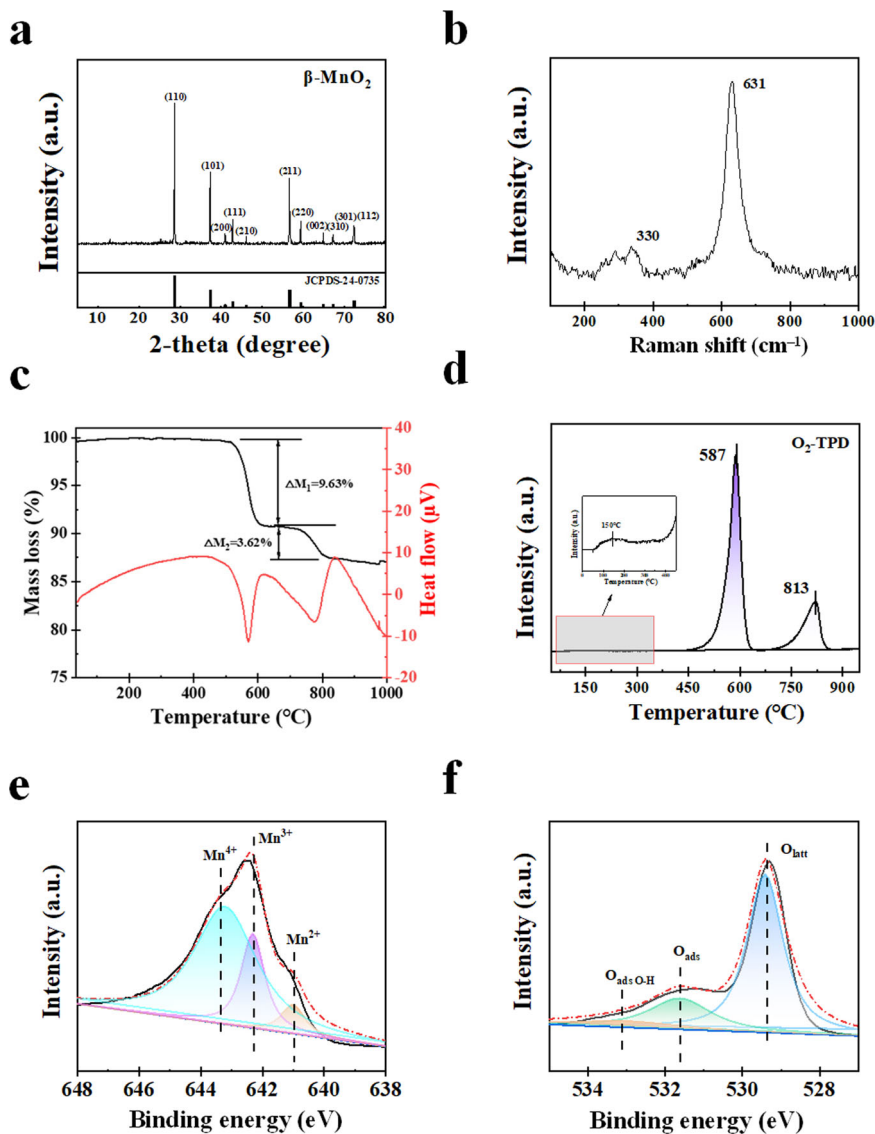


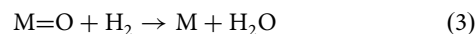
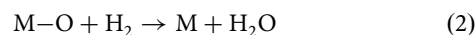
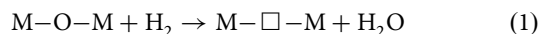
**Fig. 1** Catalyst characterization of  $\beta$ - $\text{MnO}_2$ . **a** XRD patterns. **b** Raman spectrum. **c** TG profile. **d**  $\text{O}_2$ -TPD profile. **e** Mn2p XPS spectrum. **f** O1s XPS spectrum.

**Table 1** Mn2p, O1s binding energies, and the corresponding parameters.

Elements	Assignment	Peak position (eV)	Fraction (%)
Mn2p	$\text{Mn}^{3+}$	642.3	32.0
	$\text{Mn}^{4+}$	643.4	68.0
O1s	$\text{O}_{\text{latt}}$	529.2	77.2
	$\text{O}_{\text{ads}}$	531.7	16.2
	$(\text{OH})_{\text{ads}}$	533.2	6.6

At a temperature higher than 110 °C,  $\text{H}_2\text{O}$  MS signal increases obviously (Fig. 2c) and the normalized intensity of  $\text{M}^+-\text{O}^{2-}-\text{M}^+$  ( $\text{M}-\text{O}-\text{M}$ ) decreases (Fig. 2d), but the normalized intensity of other surface oxygen species do not change significantly below 110 °C. This finding implies that the bridge-type of oxygen atom in  $\text{M}^+-\text{O}^{2-}-\text{M}^+$  ( $\text{M}-\text{O}-\text{M}$ ) first reacts with  $\text{H}_2$  to form gaseous  $\text{H}_2\text{O}$  and bridge-type OV ( $\text{M}-\square-\text{M}$ , where, OV is represented by an empty square  $\square$ ) (Eq. (1)). When the temperature exceeds 150 °C, except  $\text{M}^+-\text{O}^{2-}-\text{M}^+$ , the normalized intensities of

$\text{M}^+-\text{O}_2^-$ ,  $\text{M}^{2+}-\text{O}_2^-$ ,  $\text{M}^+-\text{O}^-$ , and  $\nu(\text{OH})$  decrease, but the normalized intensities of  $\delta(\text{H}_2\text{O})$  and  $\text{M}^{2+}-\text{O}_2^{2-}$  increase with increasing temperature. These results indicate that  $\text{M}^+-\text{O}^-$  ( $\text{M}-\text{O}$ ) and  $\text{M}^{2+}-\text{O}_2^{2-}$  ( $\text{M}=\text{O}$ ) can react with  $\text{H}_2$  above 150 °C to generate  $\text{H}_2\text{O}$  and terminal-type OV (bare M) (Eqs. (2) and (3)), which leads to an increase in the normalized intensity of  $\delta(\text{H}_2\text{O})$ <sup>47</sup>.  $\text{M}^{2+}-\text{O}_2^{2-}$  ( $\text{M}=\text{O}$ ) reacts with surface  $\text{H}_2\text{O}$  to form OH (Eq. (4)), which leads to a decrease in the normalized intensity of  $\nu(\text{OH})$  in  $\text{H}_2\text{O}$  at  $\beta$ - $\text{MnO}_2$  surfaces.



It is interesting that the normalized intensity of  $\text{M}^{2+}-\text{O}_2^{2-}$  increases with increasing temperature even in the absence of  $\text{O}_2$  (Fig. 2d). The relation of normalized intensities of  $\text{M}^{2+}-\text{O}_2^{2-}$  and  $\text{M}^{2+}-\text{O}_2^-$  is correlated (Supplementary Fig. S5). It was found

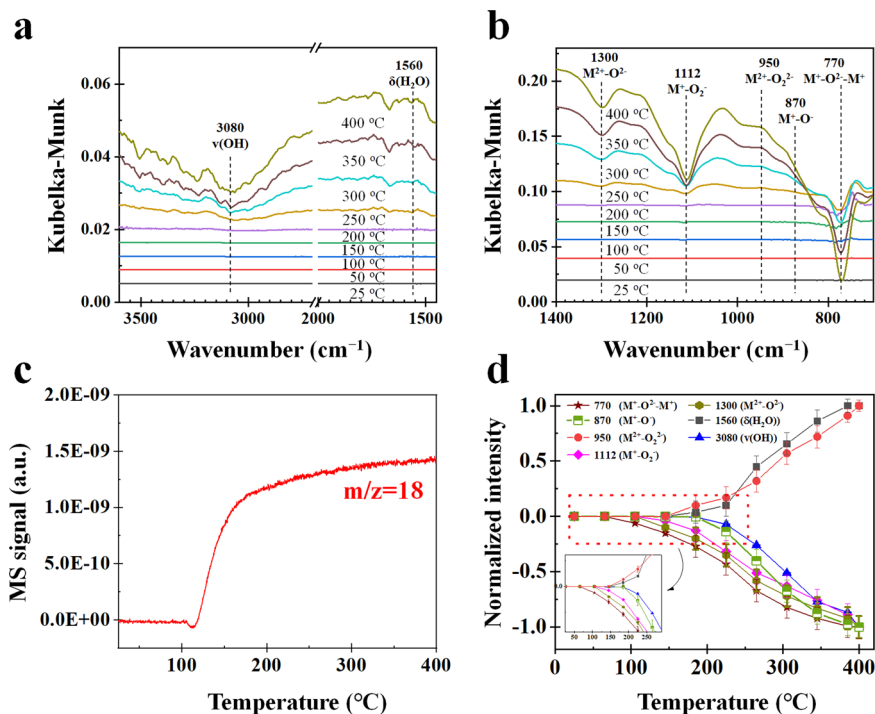
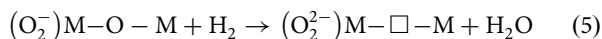
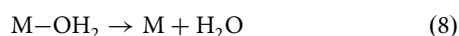
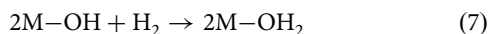
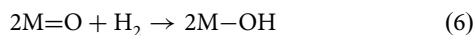


**Fig. 2** Experimental results of  $\text{H}_2$  oxidation by oxygen species at  $\beta\text{-MnO}_2$  surfaces in  $\text{H}_2/\text{Ar}$  as a function of temperature. **a**, **b** DRIFTS spectra. **c** MS signal. **d** Normalized intensities where the error bars are the standard deviations obtained by measuring the peak heights more than three times.

that a standard deviation ( $R^2$ ) of the relation is 0.965, which clearly indicates that the normalized intensity of  $\text{M}^{2+}\text{-O}_2^{2-}$  is strongly correlated with that of  $\text{M}^+\text{-O}_2^-$ . Li et al. also reported similar phenomena<sup>48</sup>. The conversion reaction between  $\text{M}^{2+}\text{-O}_2^-$  and  $\text{M}^{2+}\text{-O}_2^{2-}$  is shown in Eq. (5), where the valence state of the M cation in  $\text{M}^+\text{-O}_2^-$  is kept constant via  $\text{M}^+\text{-O}_2^-$  conversion to  $\text{M}^{2+}\text{-O}_2^{2-}$  after the formation of  $\text{M}\text{-}\square\text{-M}$ .



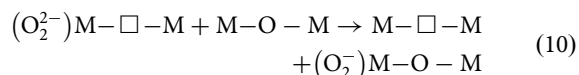
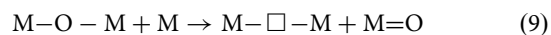
**$\text{H}_2$  oxidation by surface oxygen species in the presence of  $\text{O}_2$ .** The DRIFTS spectra, MS signals, and normalized intensities during  $\text{H}_2$  oxidation by oxygen species at  $\beta\text{-MnO}_2$  surfaces in the presence of  $\text{O}_2$  are presented in Fig. 3. The primary difference due to the presence of  $\text{O}_2$  is that the normalized intensity of  $\nu(\text{OH})$  increases with temperature in the presence of  $\text{O}_2$  (Fig. 3d), but decreases in the absence of  $\text{O}_2$  (Fig. 2d). It is also noted that  $\text{H}_2\text{O}$  MS signal ( $3.0\text{E-}09$ ) at  $400^\circ\text{C}$  in the presence of  $\text{O}_2$  (Fig. 3c) is much stronger than that ( $1.48\text{E-}09$ ) in Fig. 2c in the absence of  $\text{O}_2$ . These differences in the normalized intensity of  $\nu(\text{OH})$  trend and  $\text{H}_2\text{O}$  MS signal are evidence of  $\text{O}_2$  involvement in  $\text{H}_2$  oxidation.  $\text{O}_2$  can promote not only the release of O in  $\text{M}^+\text{-O}_2^{2-}\text{-M}^+$  (Eq. (1)) but also the formation rate of  $\text{M}\text{-OH}$  from  $\text{M}^{2+}\text{-O}_2^{2-}$  (Eq. (6)). With the increase in temperature,  $\text{M}\text{-OH}$  reacts with  $\text{H}_2$  (Eq. (7)) to form surface adsorption of  $\text{H}_2\text{O}$  that desorbs into gaseous  $\text{H}_2\text{O}$  at  $250^\circ\text{C}$  (Eq. (8))<sup>49</sup>, resulting in the formation of terminal vacancies (bare Mn).



**Regeneration of  $\text{H}_2$ -reduced  $\beta\text{-MnO}_2$  with Ar or  $\text{O}_2$ .** The fact that the normalized intensities of  $\text{M}^+\text{-O}_2^{2-}\text{-M}^+$  and  $\text{M}^{2+}\text{-O}_2^{2-}$  are all negative during  $\text{H}_2$  oxidation in both  $\text{H}_2/\text{Ar}$  and  $(\text{H}_2 + \text{O}_2)$  atmospheres (Figs. 2 and 3) indicates that OV's ( $\text{M}\text{-}\square\text{-M}$  and  $\text{M}$ )

can be generated even in the presence of  $\text{O}_2$ . A similar result has been reported by Sun et al., where they found that  $\text{M}^+\text{-O}_2^{2-}\text{-M}^+$  and  $\text{M}^{2+}\text{-O}_2^{2-}$  can be reduced by CO on  $\text{ZnO}$ <sup>50</sup>. The generation of the  $\text{M}\text{-}\square\text{-M}$  and  $\text{M}$  may be due to either the decomposition rate of  $\text{O}_2$  at  $\beta\text{-MnO}_2$  surfaces is less than that of  $\text{H}_2$  oxidation or  $\text{M}\text{-}\square\text{-M}$  and  $\text{M}$  cannot be regenerated. This issue was evaluated by conducting successive regeneration experiments in an Ar or  $\text{O}_2/\text{Ar}$  atmosphere (Supplementary Table S2).  $\beta\text{-MnO}_2$  was first reduced by  $\text{H}_2$  in the TPR cell at  $200^\circ\text{C}$  for 10 min, the regeneration was then carried out in an Ar or  $\text{O}_2/\text{Ar}$  atmosphere by elevating the temperature from  $25^\circ\text{C}$  to  $400^\circ\text{C}$ .

DRIFTS spectra and normalized intensities at various temperatures during the regeneration of  $\text{H}_2$ -reduced  $\beta\text{-MnO}_2$  in the Ar atmosphere are presented in Fig. 4. When increasing temperature from  $25^\circ\text{C}$  to  $300^\circ\text{C}$ , the normalized intensity of  $\text{M}^{2+}\text{-O}_2^{2-}$  decreases rapidly to zero, while those of  $\text{M}^{2+}\text{-O}_2^-$  and  $\text{M}^+\text{-O}_2^-$  increase rapidly to zero (Fig. 4b). The normalized intensities of  $\text{M}^+\text{-O}_2^{2-}\text{-M}^+$  and  $\text{M}^+\text{-O}^-$  asymptotically approach to  $-1.0$  at a temperature close to  $400^\circ\text{C}$ . This finding indicated that O atoms in  $\text{M}^+\text{-O}_2^{2-}\text{-M}^+$  and  $\text{O}_2$  molecules in  $\text{M}^{2+}\text{-O}_2^{2-}$  can migrate on  $\beta\text{-MnO}_2$  surfaces (Eqs. (9) and (10))<sup>32</sup>.



DRIFTS spectra and normalized intensities at various temperatures during the regeneration of  $\text{H}_2$ -reduced  $\beta\text{-MnO}_2$  in the  $\text{O}_2/\text{Ar}$  atmosphere are illustrated in Fig. 5. The normalized intensity of  $\text{M}^+\text{-O}_2^{2-}\text{-M}^+$  increases from a temperature higher than  $100^\circ\text{C}$ , indicating that the regeneration of  $\text{M}^+\text{-O}_2^{2-}\text{-M}^+$  from  $\text{M}\text{-}\square\text{-M}$  and  $\text{O}_2$  requires a temperature higher than  $100^\circ\text{C}$ <sup>51,52</sup>. Furthermore, the normalized intensity of  $\text{M}^+\text{-O}_2^{2-}\text{-M}^+$  becomes positive at temperatures greater than  $250^\circ\text{C}$ , at which all other surface oxygen species increase or decrease to 0.0, suggesting all other surface oxygen species have been completely

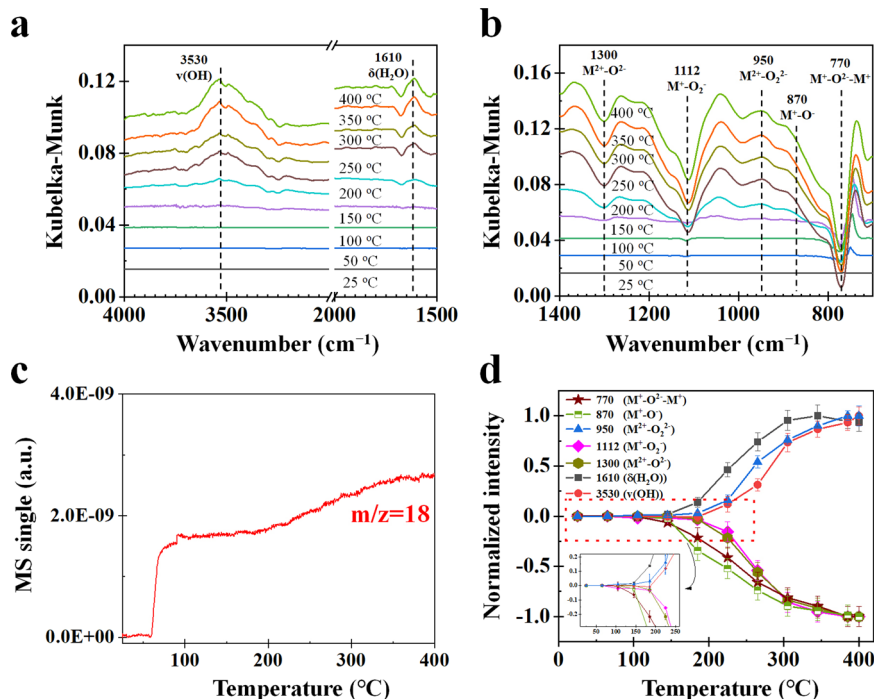


**Fig. 3** Experimental results of  $\text{H}_2$  oxidation by oxygen species at  $\beta\text{-MnO}_2$  surfaces in ( $\text{H}_2 + \text{O}_2$ ) as a function of temperature. **a, b** DRIFTS spectra. **c** MS signal. **d** Normalized intensities where the error bars are the standard deviations obtained by measuring the peak heights more than three times.

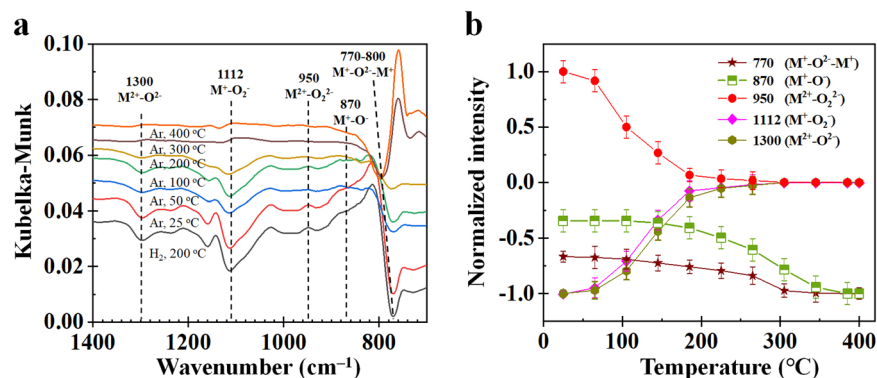


**Fig. 4** Experimental results of the regeneration of  $\text{H}_2$ -reduced  $\beta\text{-MnO}_2$  in Ar at various temperatures. **a** DRIFTS spectra. **b** normalized intensities where the error bars are the standard deviations obtained by measuring the peak heights more than three times.

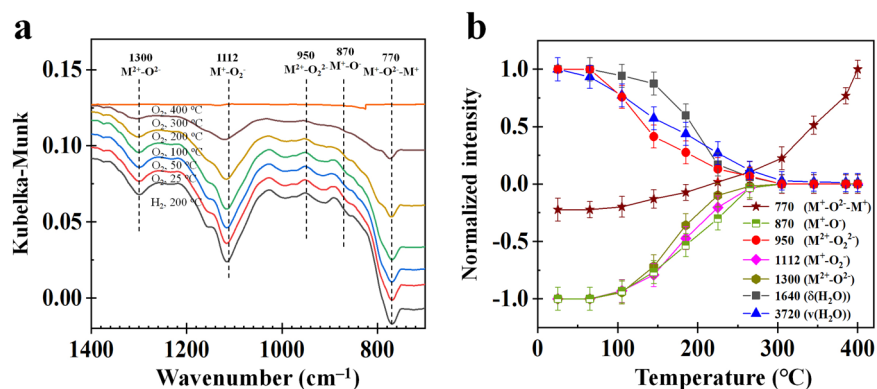


**Fig. 5** Experimental results of the regeneration of  $\text{H}_2$ -reduced  $\beta\text{-MnO}_2$  in  $\text{O}_2/\text{Ar}$  at various temperatures. **a** DRIFTS spectra. **b** normalized intensities where the error bars are the standard deviations obtained by measuring the peak heights more than three times.

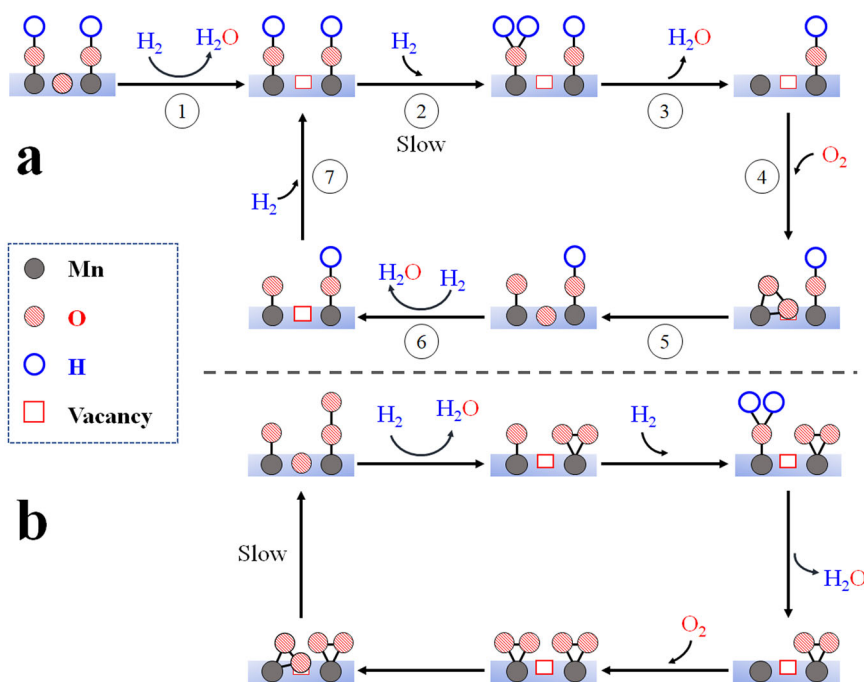
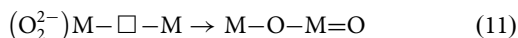


**Fig. 6** Roles and mechanisms of surface oxygen species and OV in  $\text{H}_2$  oxidation at  $\beta\text{-MnO}_2$  surfaces. **a**  $\text{H}_2$  oxidation between 110 and 150 °C. **b**  $\text{H}_2$  oxidation at a temperature higher than 150 °C.

regenerated. We may further note that  $\text{M}^+-\text{O}^{2-}-\text{M}^+$  can convert to  $\text{M}^{2+}-\text{O}^{2-}$  (Eq. (9)). From the fact that the normalized intensity of  $\text{M}^{2+}-\text{O}^{2-}$  increases little at temperatures greater than 250 °C but that of  $\text{M}^+-\text{O}^{2-}-\text{M}^+$  increases significantly, these findings deduce that the reaction in Eq. (9) is reversible.

The decreases in normalized intensities of  $\delta(\text{H}_2\text{O})$  and  $\nu(\text{OH})$  indicate that  $\text{H}_2\text{O}$  can desorb from  $\text{M}-\text{OH}_2$  and  $\text{M}-\text{OH}$  at  $\beta\text{-MnO}_2$  surface, resulting in the formation of bare M.

**Roles of OVs in  $\text{H}_2$  catalytic oxidation.** The roles of OVs in  $\text{H}_2$  oxidation process at  $\beta\text{-MnO}_2$  surfaces in the presence of  $\text{O}_2$  can be deduced from the above discussion, and the proposed mechanism is illustrated in Fig. 6. First, when the reaction temperature is in a range of 110–150 °C, the oxygen atom in the bridge-type  $\text{M}^+-\text{O}^{2-}-\text{M}^+$  can react with  $\text{H}_2$  to form  $\text{H}_2\text{O}$  and OV via steps (1) and (6) in Fig. 6a. According to steps (2) and (7), the oxygen atoms in the terminal-type  $\text{M}^{2+}-\text{O}^{2-}$  and  $\text{M}-\text{OH}$  react with  $\text{H}_2$  to generate surface  $\text{M}-\text{OH}$  and gaseous  $\text{H}_2\text{O}$ . The gaseous  $\text{O}_2$  adsorbed at the bare M site in  $\text{M}^+-\square-\text{M}^+$  (step (4)) yields  $\text{M}^{2+}-\text{O}_2^{2-}$ .  $\text{M}^{2+}-\text{O}_2^{2-}$  dissociates simultaneously to  $\text{M}^+-\text{O}^{2-}-\text{M}^+$  and  $\text{M}^{2+}-\text{O}^{2-}$  (step (5), Eq. (11)). We can only find the decrease in  $\text{M}^+-\text{O}^{2-}-\text{M}^+$  and increase in  $\text{M}-\square-\text{M}$  in this temperature range as the step (2) is rate limited reaction.



As the oxidation process in Fig. 6b, when the temperature is above 150 °C, OH in  $\text{M}-\text{OH}$  becomes reactive enough, the  $\text{O}_2$  dissociation step (6) is slowest, resulting in the accumulation of  $\text{M}-\square-\text{M}$  and  $\text{M}^{2+}-\text{O}_2^{2-}$ .

**Conclusion.** We explored  $\text{O}_2$  dissociation, OVs formation, and surface oxygen species conversion during  $\text{H}_2$  oxidation at  $\beta\text{-MnO}_2$  surface using the operando TPR-DRIFTS-MS technology. The results demonstrate that the operando TPR-DRIFTS-MS technology employed herein is a highly useful tool for identifying OVs at  $\beta\text{-MnO}_2$  surfaces and  $\text{CeO}_2$  and  $\text{Co}_3\text{O}_4$  surfaces (Supplementary Fig. S6), and for understanding the roles of OVs and

oxygen species in catalytic processes. In particular, the difference in the reaction characteristics of bridge-type ( $\text{M}^+-\text{O}^{2-}-\text{M}^+$ ) and terminal-type ( $\text{M}^{2+}-\text{O}^{2-}$ ) oxygen species can be clearly observed using the operando TPR-DRIFTS-MS technology. Accordingly, we expect this technology could provide an important characterization method to understand the roles of surface oxygen species on metal oxide catalysts and enable the rational design of catalysts of OVs with satisfied performance.

## Methods

**Materials.**  $\beta\text{-MnO}_2$  (99%) was purchased from Aladdin, Shanghai, China. Pure Ar (99.999%), pure  $\text{O}_2$  (99.999%), 5 vol%  $\text{H}_2$  standard gas (Ar balanced), and 5 vol% CO standard gas (Ar balanced) were purchased from Huayang, Changzhou, China.

**Catalyst characterization.** Physicochemical properties of  $\beta\text{-MnO}_2$  were characterized by via various techniques, such as X-ray powder diffraction (XRD), thermogravimetric (TG) analysis, Raman, X-ray photoelectron spectroscopy (XPS), oxygen temperature-programmed desorption ( $\text{O}_2$ -TPD), and high-resolution transmission electron microscopy (HRTEM).

**DRIFTS-MS system.** A schematic diagram of the operando TPR-DRIFTS-MS system is shown in Supplementary Fig. S7. The system consisted of gas cylinders, gas flow meters (MFC, D07, Sevenstars Beijing, China), operando DRIFTS (Nicolet 50, Thermo Scientific, USA), and MS (Tilon LC-D200M, Ametek, USA). The DRIFTS was equipped with a TPR cell (HVC-DRP-5, Harrick, USA) and a narrow-band mercury cadmium telluride (MCT-A) detector with liquid nitrogen cooling for high sensitivity ( $0.09 \text{ cm}^{-1}$ ) in collecting DRIFTS spectra between 4000 and  $650 \text{ cm}^{-1}$ .

For the DRIFTS spectrum collection experiment,  $\beta\text{-MnO}_2$  powders were pretreated for 1 h in Ar at 450 °C (20 mL/min). Then, the  $\beta\text{-MnO}_2$  powders were cooled to room temperature and stabilized for 10 min, and DRIFTS background spectra were collected. The gas mixture (Supplementary Table S2) was supplied into the TPR cell for 20 min. The  $\beta\text{-MnO}_2$  powder temperature was elevated with programmed heating using a temperature controller. Series software was used to collect the corresponding spectra. Thirty-two scans were performed with a resolution of  $4 \text{ cm}^{-1}$ , and the spectrum data of DRIFTS were analyzed using OMNIC software during the acquisition. The Kubelka–Munk function was used to convert the obtained spectra into absorption spectra, whose intensities were linearly related to the amount of adsorption. The gas from the TPR cell was analyzed using mass spectrometer (MS) (Tilon, LC-D200M, Ametek, USA) to obtain signals of  $\text{H}_2$  ( $m/z = 2$ ),  $\text{H}_2\text{O}$  ( $m/z = 18$ ),  $\text{O}_2$  ( $m/z = 32$ ), and Ar ( $m/z = 40$ ).

**Normalization of peak intensity.** The collected infrared spectra at different temperatures were normalized for relatively quantitative analysis. The normalization was calculated using Eqs. (12) and (13) based on the absolute values of the highest height ( $P_{i\max}$ ) for positive peaks and lowest peak height ( $P_{i\min}$ ) for negative peaks, respectively.

$$N_i = \frac{P_i}{P_{i\max}} \quad (12)$$

$$N_i = \frac{P_i}{|P_{i\min}|} \quad (13)$$

$N_i$  represents the normalized intensity of the absorption peak  $i$  at the corresponding temperature;  $P_i$  represents the peak height of the absorption peak  $i$  at the corresponding temperature.

## Data availability

Data will be made available on request.

Received: 23 February 2022; Accepted: 8 August 2022;

Published online: 20 August 2022

## References

- Gurylev, V., Su, C. & Perng, T. Surface reconstruction, oxygen vacancy distribution and photocatalytic activity of hydrogenated titanium oxide thin film. *J. Catal.* **330**, 177–186 (2015).
- Fan, X. et al. Oxygen-deficient three-dimensional porous  $\text{Co}_3\text{O}_4$  nanowires as an electrode material for water oxidation and energy storage. *ChemElectroChem* **4**, 2453–2459 (2017).
- Xiong, J. et al. Surface defect engineering in 2D nanomaterials for photocatalysis. *Adv. Funct. Mater.* **28**, 1801983 (2018).
- Wang, G. et al. Oxygen defective metal oxides for energy conversion and storage. *Nano Today* **13**, 23–39 (2017).
- Mars, P. & van Krevelen, D. Oxidations carried out by means of vanadium oxide catalysts. *Chem. Eng. Sci.* **3**, 41–59 (1954).
- Over, H. et al. Atomic-scale structure and catalytic reactivity of the  $\text{RuO}_2(110)$  surface. *Science* **287**, 1474–1476 (2000).
- Schaub, R. et al. Oxygen-mediated diffusion of oxygen vacancies on the  $\text{TiO}_2(110)$  surface. *Science* **299**, 377–379 (2003).
- Haber, J. et al. Vanadium pentoxide. I. Structures and properties. *Appl. Catal. A-Gen.* **157**, 3–22 (1997).
- Esch, F. et al. Electron localization determines defect formation on ceria substrates. *Science* **309**, 752–755 (2005).
- Anpo, M. et al. Characterisation and reactivity of oxygen species at the surface of metal oxides. *J. Catal.* **393**, 259–280 (2021).
- Ye, K. et al. An overview of advanced methods for the characterization of oxygen vacancies in materials. *Trend Anal. Chem.* **116**, 102–108 (2019).
- Epling, W. et al. Evidence for oxygen adatoms on  $\text{TiO}_2(110)$  resulting from  $\text{O}_2$  dissociation at vacancy sites. *Surf. Sci.* **412/413**, 333–343 (1998).
- Zhuang, G. et al. Oxygen vacancies in metal oxides: recent progress towards advanced catalyst design. *Sci. China Mater.* **63**, 2089–2118 (2020).
- Solakidou, M. et al. Efficient photocatalytic water-splitting performance by ternary  $\text{CdS/Pt-N-TiO}_2$  and  $\text{CdS/Pt-N, F-TiO}_2$ : interplay between  $\text{CdS}$  photo corrosion and  $\text{TiO}_2$ -doping. *Appl. Catal. B-Environ.* **254**, 194–205 (2019).
- Yu, K. et al. Asymmetric oxygen vacancies: the intrinsic redox active sites in metal oxide catalysts. *Adv. Sci.* **7**, 1901970 (2020).
- Dong, L. et al. Study of the properties of  $\text{CuO/VO}_x/\text{Ti}_{0.5}\text{Sn}_{0.5}\text{O}_2$  catalysts and their activities in  $\text{NO} + \text{CO}$  reaction. *ACS Catal.* **1**, 468–480 (2011).
- Nie, L. et al. Activation of surface lattice oxygen in single-atom  $\text{Pt/CeO}_2$  for low-temperature  $\text{CO}$  oxidation. *Science* **358**, 1419–1423 (2017).
- Wan, P. et al. Elucidating structure-performance correlations in gas-phase selective ethanol oxidation and  $\text{CO}$  oxidation over metal-doped  $\gamma\text{-MnO}_2$ . *Chin. J. Catal.* **41**, 1298–1310 (2020).
- Kong, X. et al. Oxygen vacancy induced  $\text{Bi}_2\text{WO}_6$  for the realization of photocatalytic  $\text{CO}_2$  reduction over the full solar spectrum: from the UV to the NIR region. *Chem. Commun.* **52**, 14242–14245 (2016).
- Wu, J. et al. Efficient visible-light-driven  $\text{CO}_2$  reduction mediated by defect-engineered  $\text{BiOBr}$  atomic layers. *Angew. Chem.* **130**, 8855–8859 (2018).
- Huang, Y. et al. Efficient charges separation using advanced  $\text{BiOI}$ -based hollow spheres decorated with palladium and manganese dioxide nanoparticles. *Angew. Chem.* **57**, 122–138 (2018).
- Mo, S. et al. Unraveling the decisive role of surface  $\text{CeO}_2$  nanoparticles in the  $\text{Pt-CeO}_2/\text{MnO}_2$  hetero-catalysts for boosting toluene oxidation: Synergistic effect of surface decorated and intrinsic O-vacancies. *Chem. Eng. J.* **418**, 129399 (2021).
- Yang, W. et al. Comparative study of  $\alpha$ -,  $\beta$ -,  $\gamma$ - and  $\delta$ - $\text{MnO}_2$  on toluene oxidation: oxygen vacancies and reaction intermediates. *Appl. Catal. B-Environ.* **260**, 118150 (2020).
- Mao, L. et al. Plasma-catalyst hybrid reactor with  $\text{CeO}_2/\gamma\text{-Al}_2\text{O}_3$  for benzene decomposition with synergetic effect and nano particle by-product reduction. *J. Hazard. Mater.* **347**, 150–159 (2018).
- Huang, J. et al. Effect of  $\text{MnO}_2$  phase structure on the oxidative reactivity toward bisphenol A degradation. *Environ. Sci. Technol.* **52**, 11309–11318 (2018).
- Duan, X. et al. Controllable hydrothermal synthesis of manganese dioxide nanostructures: shape evolution, growth mechanism and electrochemical properties. *CrystEngComm* **14**, 4196–4204 (2012).
- Kong, F. et al. Insight into the crystal structures and surface property of manganese oxide on  $\text{CO}$  catalytic oxidation performance. *Inorg. Chem.* **60**, 5812–5820 (2021).
- Yamaguchi, Y. et al. Template-free synthesis of mesoporous  $\beta\text{-MnO}_2$  nanoparticles structure, formation mechanism, and catalytic properties. *ACS Appl. Mater. Inter.* **12**, 36004–36013 (2020).
- Yao, W. et al. Cations controlled growth of  $\beta\text{-MnO}_2$  crystals with tunable facets for electrochemical energy storage. *Nano Energy* **48**, 301–311 (2018).
- Zhang, J. et al. Crystallization design of  $\text{MnO}_2$  towards better supercapacitance. *CrystEngComm* **14**, 5892–5897 (2012).
- Cheng, G. et al. A facile one-pot hydrothermal synthesis of  $\beta\text{-MnO}_2$  nanopincers and their catalytic degradation of methylene blue. *J. Solid. State Chem.* **217**, 57–63 (2014).
- Zhou, G. et al. Degradation of organic pollutants by peroxymonosulfate activated by  $\text{MnO}_2$  with different crystalline structures: Catalytic performances and mechanisms. *Chem. Eng. J.* **374**, 170–180 (2019).
- Dong, L. et al. Synergy of Mn and Ni enhanced catalytic performance for toluene combustion over Ni-doped  $\alpha\text{-MnO}_2$  catalysts. *Chem. Eng. J.* **388**, 124244 (2020).
- Liu, Y. et al. Facile and green synthetic strategy of birnessite-type  $\text{MnO}_2$  with high efficiency for airborne benzene removal at low temperatures. *Appl. Catal. B-Environ.* **245**, 569–582 (2019).
- Liu, C. et al. Effects of  $\text{MnO}_2$  crystal structure on the sorption and oxidative reactivity toward thallium(I). *Chem. Eng. J.* **416**, 127919 (2021).
- Pan, T. et al. Facile homogeneous precipitation method to prepare  $\text{MnO}_2$  with high performance in catalytic oxidation of ethyl acetate. *Chem. Eng. J.* **417**, 129246 (2021).
- Panov, G., Dubkov, K. & Starokon, E. Active oxygen in selective oxidation catalysis. *Catal. Today* **117**, 148–155 (2006).
- Wu, J. et al. In situ DRIFTS study of  $\text{O}_3$  adsorption on  $\text{CaO}$ ,  $\gamma\text{-Al}_2\text{O}_3$ ,  $\text{CuO}$ ,  $\alpha\text{-Fe}_2\text{O}_3$  and  $\text{ZnO}$  at room temperature for the catalytic ozonation of cinnamaldehyde. *Appl. Surf. Sci.* **412**, 290–305 (2017).
- Brodu, N. et al. Role of Lewis acid sites of ZSM-5 zeolite on gaseous ozone abatement. *Chem. Eng. J.* **231**, 281–286 (2013).
- Roscoe, J. & Abbott, J. Diffuse reflectance FTIR study of the interaction of alumina surfaces with ozone and water vapor. *J. Phys. Chem. A.* **109**, 9028–9034 (2005).
- Larson, V. et al. Iron and manganese oxo complexes, oxo wall and beyond. *Nat. Rev. Chem.* **4**, 404 (2020).
- Li, C., Domen, K. & Maruya, K. Oxygen exchange reactions over cerium oxide: an FT-IR study. *J. Catal.* **123**, 436–442 (1990).
- Jiang, S. et al. Insight into the reaction mechanism of  $\text{CO}_2$  activation for  $\text{CH}_4$  reforming over  $\text{NiO-MgO}$ : a combination of DRIFTS and DFT study. *Appl. Surf. Sci.* **416**, 59–68 (2017).
- Luca, B., Alfonso, P. & Maria, C.  $\text{O}_2$  activation over Ag-decorated  $\text{CeO}_2(111)$  and  $\text{TiO}_2(110)$  surfaces: a theoretical comparative investigation. *J. Phys. Chem. C.* **124**, 25917–25930 (2020).
- TheoKlopogge, J. et al. XPS study of the major minerals in bauxite: gibbsite, bayerite and (pseudo-) boehmite. *J. Colloid Interf. Sci.* **296**, 572–576 (2006).
- Gonzalez, P. & Calatayud, M. Toward an understanding of the hydrogenation reaction of  $\text{MO}_2$  gas-phase clusters ( $M = \text{Ti, Zr, and Hf}$ ). *J. Phys. Chem. C.* **117**, 5354–5364 (2013).
- Selasteen, F. et al. Structural, spectral, optical, thermal and Z-Scan potential studies of copper sodium tartrate single crystal for higher order nonlinear optical applications. *Optik* **168**, 231–240 (2019).
- Li, C. et al. Dioxygen adsorption on well-outgassed and partially reduced cerium oxide studied by FT-IR. *J. Am. Chem. Soc.* **111**, 7683–7687 (1989).
- Qin, Y. et al. Evolution and enhancement of the oxygen cycle in the catalytic performance of total toluene oxidation over manganese-based catalysts. *J. Catal.* **380**, 21–31 (2019).
- Sun, Y. et al. Tailoring active  $\text{O}_2^-$  and  $\text{O}_2^{2-}$  anions on a  $\text{ZnO}$  surface with the addition of different alkali metals probed by  $\text{CO}$  oxidation. *Ind. Eng. Chem. Res.* **59**, 9382–9392 (2020).
- Brugnoli, L. et al.  $\text{O}_2$  activation over Ag-decorated  $\text{CeO}_2(111)$  and  $\text{TiO}_2(110)$  surfaces: a theoretical comparative investigation. *J. Phys. Chem. C.* **124**, 25917–25930 (2020).

52. Williams, O. & Sievers, C. Active oxygen species in heterogeneously catalyzed oxidation reactions. *Appl. Catal. A-Gen.* **614**, 118057 (2021).

### Acknowledgements

This work was supported by the National Natural Science Foundation of China (12075037) and Research and Application Service Platform Project of API Manufacturing Environmental Protection and Safety Technology in China (2020-0107-3-1).

### Author contributions

J.X., T.Z., and S.F. carried out experiments and wrote the manuscript. S.Y. designed the study and interpreted the results. J.L., E.G., W.W., and J.Z. provided the experimental scheme and wrote the manuscript. Z.W. provided the experimental scheme and discussion.

### Competing interests

The authors declare no competing interests.

### Additional information

**Supplementary information** The online version contains supplementary material available at <https://doi.org/10.1038/s42004-022-00717-0>.

**Correspondence** and requests for materials should be addressed to Shuiliang Yao.

**Peer review information** *Communications Chemistry* thanks the anonymous reviewers for their contribution to the peer review of this work.

**Reprints and permission information** is available at <http://www.nature.com/reprints>

**Publisher's note** Springer Nature remains neutral with regard to jurisdictional claims in published maps and institutional affiliations.



**Open Access** This article is licensed under a Creative Commons Attribution 4.0 International License, which permits use, sharing, adaptation, distribution and reproduction in any medium or format, as long as you give appropriate credit to the original author(s) and the source, provide a link to the Creative Commons license, and indicate if changes were made. The images or other third party material in this article are included in the article's Creative Commons license, unless indicated otherwise in a credit line to the material. If material is not included in the article's Creative Commons license and your intended use is not permitted by statutory regulation or exceeds the permitted use, you will need to obtain permission directly from the copyright holder. To view a copy of this license, visit <http://creativecommons.org/licenses/by/4.0/>.

© The Author(s) 2022